JGR Solid Earth

RESEARCH ARTICLE
10.1029/2018JB016576

Special Section:
Magnetism in the Geosciences - Advances and Perspectives

Diagenetic Fate of Biogenic Soft and Hard Magnetite in Chemically Stratified Sedimentary Environments of Mamanguá Ría, Brazil

D. Rodelli[1], L. Jovane[1], M. Giorgioni[1,2], E. S. Rego[1,3], F. Cornaggia[1], M. Benites[1], P. Cedraz[1], G. B. B. Berbel[1], E. S. Braga[1], A. Ustra[4], F. Abreu[5], and A. P. Roberts[6]

[1]Instituto Oceanográfico, Universidade de São Paulo, São Paulo, Brazil, [2]Instituto de Geociências, Universidade de Brasília, Brasília, Brazil, [3]Instituto de Geociências, Universidade de São Paulo, São Paulo, Brazil, [4]Instituto de Astronomia, Geofísica e Ciências Atmosféricas, Universidade de São Paulo, São Paulo, Brazil, [5]Instituto de Microbiologia Paulo de Góes, Universidade Federal do Rio de Janeiro, Rio de Janeiro, Brazil, [6]Research School of Earth Sciences, Australian National University, Canberra, ACT, Australia

Abstract Magnetotactic bacteria (MTB) synthesize magnetite and greigite crystals under low oxygen conditions in the water column or uppermost sediment (greigite-producing bacteria are found below the oxic-anoxic transition). Dissolved iron and oxygen contents in local environments are known to be limiting factors for the production and preservation of biogenic magnetite. Understanding the processes that link MTB to their living environments is fundamental to reconstructing past chemical variations in the water column and sediment, and for using the magnetic properties of biogenic magnetite as environmental proxy indicators. Previous studies have suggested that the frequently identified biogenic soft (BS) and biogenic hard (BH) magnetite types are associated with equant and more elongated morphologies, respectively, and that their abundance varies in accordance with sedimentary oxygen content, where MTB that produce the BH component live in less oxygenated environments. We test this hypothesis in a high-resolution integrated environmental magnetic and geochemical study of surface sediments from Mamanguá Ría, SE Brazil. Based on magnetic and pore water profiles, we demonstrate that both the BS and BH components occur within microaerobic environments and that as sediment oxygen content decreases with depth, the BS component disappears before the BH component. With continued burial into the sulfidic diagenetic zone, both components undergo progressive dissolution, but the BH component is more resistant to dissolution than the BS component. Our observations confirm previous inferences about the relative stability of these phases and provide a firmer basis for use of these two types of biogenic magnetite as paleoenvironmental proxies.

Key Points:
- We demonstrate that biogenic magnetite production is controlled by pore water oxygen concentration and redox potential in sediments
- Progressive dissolution of biogenic magnetite occurs at the sulfate–methane transition where magnetite becomes unstable
- The biogenic *hard* component is slightly more resistant to dissolution than the biogenic *soft* component

Supporting Information:
- Supporting Information S1

Correspondence to:
L. Jovane,
jovane@usp.br

Citation:
Rodelli, D., Jovane, L., Giorgioni, M., Rego, E. S., Cornaggia, F., Benites, M., et al. (2019). Diagenetic fate of biogenic soft and hard magnetite in chemically stratified sedimentary environments of Mamanguá Ría, Brazil. *Journal of Geophysical Research: Solid Earth*, *124*, 2313–2330. https://doi.org/10.1029/2018JB016576

Received 21 AUG 2018
Accepted 19 FEB 2019
Accepted article online 21 FEB 2019
Published online 25 MAR 2019

1. Introduction

Magnetotactic bacteria (MTB) are a group of prokaryotes that biosynthesize membrane-bound magnetic mineral crystals (Bazylinski et al., 1995; Bazylinski & Frankel, 2004). They occur in many aquatic environments, including in freshwater, marshes, and marine waters (Yan et al., 2012), and are found commonly in water columns and sediments with vertical chemical stratification (Bazylinski & Williams, 2006). The abundance of magnetite-producing MTB is generally highest around the oxic-anoxic interface (OAI; i.e., the nitrogenous-ferruginous boundary; Roberts, 2015), while greigite-producing MTB live in anoxic sulfidic regions. MTB are, therefore, considered to be facultatively anaerobic microaerophiles. MTB can occur in large numbers in specific conditions (e.g., at the OAI), which suggests that their presence is related to specific ecological conditions (Bazylinski & Williams, 2006). Therefore, studying the natural distribution of MTB can be useful for understanding water column and sedimentary environments.

Magnetite produced by MTB has specific characteristics in terms of stoichiometry, crystal structure, morphology, size, and spatial organization (Chen et al., 2014; Egli, 2004b; Kopp & Kirschvink, 2008; Mann et al., 1984; Yan et al., 2012). The magnetic properties of biogenic magnetite have been studied extensively (Chang et al., 2018; Egli, 2004a, 2004b, 2004c; Egli et al., 2010; Jovane et al., 2012; Kruiver & Passier, 2001; Mohamed et al., 2011; Moskowitz et al., 1993; Pan, Petersen, Davila, et al., 2005, Pan, Petersen, Winklhofer, et al., 2005; Roberts et al., 2011; Savian et al., 2014, 2016), and a range of techniques exist to recognize and characterize such crystals. Environmental magnetic studies can be a rapid and reliable way

to track the spatial distribution of MTB, which have the potential to enable reconstruction of oxygen gradients in natural environments (Chang et al., 2018), where other proxies or methods of study are less readily applicable. For example, previous studies have suggested that the frequently identified biogenic soft (BS) and biogenic hard (BH) magnetite types are associated with equant and more elongated morphologies, respectively, and that their abundance varies in accordance with sedimentary oxygen content, where MTB that produce the BH component live in less oxygenated environments (Chang et al., 2013, 2018; Egli, 2004a, 2004b, 2004c; Kodama et al., 2013; Usui et al., 2017; Yamazaki, 2012; Yamazaki & Shimono, 2013). Despite the potential value of such proxy information, magnetic proxies for BS and BH magnetite have not been assessed adequately in relation to direct pore water determinations of sedimentary oxygenation. The aim of this study is to provide a direct test of whether the BS and BH magnetite types can be used to provide proxy information about sedimentary oxygenation.

We present an integrated study of magnetic properties, pore water chemistry, and lithology of surface sediments from a coastal ría environment in the Saco do Mamanguá (Rio de Janeiro, Brazil) (Benites et al., 2015; Rodelli et al., 2018). A previous study of chemical and structural characteristics of extracted biogenic magnetite from Mamanguá Ría indicates that structural transformation of crystals occurs with depth, with partial oxidation of magnetite into maghemite (Rodelli et al., 2018). Beginning with this observation, our objective is to understand the interplay between physical and chemical environmental characteristics and their relation to MTB. We characterize chemical stratification in the sediment column in a small, enclosed basin, with limited oceanic influx by comparing direct (pore water chemistry, lithology) and indirect (magnetic) methods to assess whether magnetic properties can provide proxies for geochemical and oceanographic conditions in the geological record. This work represents a comprehensive analysis of the boundary conditions for geological preservation of biogenic magnetite. Our results should be helpful in gaining new insights into links between metabolic processes of MTB and their environment.

2. Environmental Setting

Saco do Mamanguá is located in Ilha Grande Bay and is part of the Municipality of Paraty (Rio de Janeiro, Brazil). It is elongated (~11-km long and ~2-km wide) and is flanked by relatively steep mountains (Figure 1). It is, thus, morphologically considered a *ría* (i.e., an ancient river valley drowned due to postglacial sea level rise, Castaing & Guilcher, 1995). Mamanguá Ría has restricted circulation and low intensity tidal variation, which ranges between 64 and 125 cm (Bernardes, 1996). The inner ría receives organic matter from land, like in an estuary, while the outer ría is influenced by marine production (Spera, 2012). Surface sediments are predominantly composed of clay and silt and are water saturated. High organic phosphorus contents (199–324 mg/g) indicate a significant nutrient supply from local soil erosion (Teixeira, 2009). Gas seepage has been reported from shallow depths below the seafloor (Benites et al., 2015).

The ría margins are composed of granites linked to the Araçuaí orogen (Almeida, 1977; Pedrosa-Soares et al., 2007). Peraluminous granites are dominant on the NE ría flank, while alkaline granites and gneissic leucogranites crop out on the SW flank. Structurally, the region is characterized by an extensive SW-NE and SE-NW oriented orthogonal fault and fracture system. Atlantic forest covers most of the area and has contributed to formation of extensive lateritic soils.

3. Materials and Methods

Sediment cores were collected at 11 sites along Mamanguá Ría during various cruises between February 2014 and August 2015. This study is focused on cores collected from Sites 1, 4, and 9, from the outer, middle, and inner sections of the ría, respectively (Figure 1 and Table 1). At Site 9, a vibracorer was used to obtain a longer core (Core 9M), which led to recovery of 411 cm of sediment. Core 9M has been studied in detail, with environmental magnetic measurements at 1-cm stratigraphic intervals and discrete samples collected at 2- or 5-cm intervals. At Sites 1, 4, and 9 (Cores 1, 4, and 9), a custom-made gravity corer was used, recovering 81, 129, and 242 cm of sediment, respectively, and the recovered material was sampled at 5-cm stratigraphic intervals to enable correlation of Core 9M to the basin. We studied only cores from three sites because of the limited variation expected in the small area of Mamanguá Ría, with cores selected to represent the outer, middle, and inner ría.

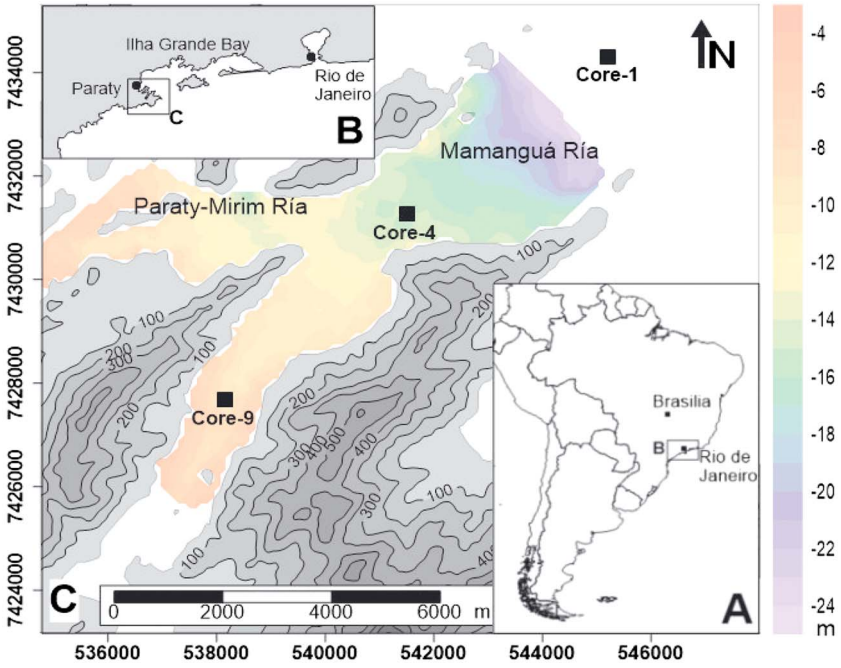

Figure 1. Map of Mamanguá Ría and surrounding areas, with the positions of the three studied sediment cores marked with black squares.

3.1. Paleomagnetism

Detailed magnetic measurements were made throughout Core 9M (411 cm) on continuous u-channel samples with 2 × 2 cm cross section and length <1.5 m (Weeks et al., 1993). Discrete oriented samples were collected at 5-cm intervals in plastic cylinders. The natural remanent magnetization (NRM) was analyzed first on the u-channel sample. To identify primary and secondary magnetic components, we used stepwise alternating field (AF) demagnetization, with steps of 0, 2.5, 5, 7.5, 10, 15, 20, 25, 30, 40, 50, 60, 70, 80, 90, and 100 mT. The u-channel was measured at 1-cm intervals, where consecutive measurements are not independent due to the 4.5-cm half-width of the response function of the 2-G Enterprises superconducting rock magnetometer used for the analyses (e.g., Weeks et al., 1993). The magnetometer is located in a magnetically shielded room at the Paleomagnetism Laboratory, Instituto de Astronomia, Geofísica e Ciências Atmosféricas, Universidade de São Paulo, Brazil. Data were analyzed with the software of Xuan and Channell (2009) to isolate the characteristic remanent magnetization, using principal component analysis (Kirschvink, 1980), and deconvolution was applied. The magnetometer response functions were measured using an internal standard. Edge effects due to the half-width of the magnetometer response function require data removal from the first and last 5 cm of each u-channel to avoid artifacts during deconvolution.

3.2. Environmental Magnetism

Various magnetic measurements were made to analyze the magnetic mineralogy of the studied cores. An anhysteretic remanent magnetization (ARM) was imparted by imposing a 0.1-mT direct current (DC) bias field while demagnetizing the sample in a 0.1 T AF. The ARM was then measured and progressively AF demagnetized with fields of 5, 10, 15, 20, 25, 30, 40, 50, 60, 70, 80, 90, and 100 mT. An isothermal remanent magnetization (IRM) was imparted by applying a 1.0 T direct field (IRM@1.0) and a backfield IRM was then imparted by subsequently applying DC fields of 0.1 T (IRM@-0.1) and 0.3 T (IRM@-0.3) in the opposite direction. U-channel ARM and IRM data were processed and deconvolved with the software of Xuan and Channell (2009). Parameters were calculated as follows: (i) *S* ratio (as IRM@-0.3/IRM@1) and (ii) Hard IRM (HIRM) (as [IRM@-0.3+IRM@1]/2) (Jovane et al., 2013; Liu et at., 2012; Verosub & Roberts, 1995).

Table 1
Latitude, Longitude, and Water Depth of the Analyzed Cores

Site	Latitude (S)	Longitude (W)	Water depth (m)
1	23°11′57″	44°33′18″	26.4
4	23°13′37″	44°35′52″	15.4
9	23°16′33″	44°38′6″	7.2

After completion of NRM, ARM, and IRM measurements on u-channel samples, cores 1, 4, and 9M were sampled at 5-cm intervals for additional magnetic analyses. The sampled sediment was then dried, milled, and sieved to retain the <150-μm fraction before the following magnetic measurements were made. Detailed IRM acquisition curves were measured by placing samples in progressively higher DC fields up to maximum fields of 1.8 T, with 100 acquisition steps, at which point the magnetization is a saturation IRM. IRM curves were separated into discrete coercivity components following Robertson & France (1994), with cumulative log-Gaussian functions using the software of Kruiver and Passier (2001). Parameters associated with each magnetic component were documented. Hysteresis loops were then measured by placing samples in an applied magnetic field that was increased progressively to a maximum value of 1.8 T and then decreased in the opposite direction to −1.8 T to determine the saturation magnetization (M_s), saturation remanence (M_r), and coercivity (B_c) for each sample. The high-field contribution was corrected using the slope of the linear part of the hysteresis loop.

First-order reversal curve (FORC) diagrams are plotted as a two-dimensional distribution function from a class of partial hysteresis curves, where one dimension represents the coercivity and the other represents magnetostatic interactions among Single Domain (SD) magnetic particles or features associated with the presence of vortex state or multidomain particles (Pike et al., 1999; Roberts et al., 2000, 2017). FORC diagrams were produced using the FORCINEL 3.0 software (Harrison & Feinberg, 2008). For samples from cores 1 and 4, low-resolution FORCs (100 curves) were measured at 5-cm stratigraphic intervals to gain preliminary information about magnetic mineral assemblages (for a total of 70 FORCs), while four selected samples from Core 9M were measured at high resolution (297 curves each, averaging time of 150 ms, $\delta B = 0.075$ mT, for five sets of stacked measurements). Low-resolution FORCs (100 curves each) were measured for samples collected at 2-cm intervals from the uppermost 50 cm of Core 9M and at 5-cm intervals throughout cores 1 and 4. Principal component analysis (PCA) was performed to separate contributions of different FORC end-members, using the FORCem algorithm of Lascu et al. (2015). FORC diagrams are an excellent method for detecting signatures due to biogenic magnetite (Egli et al., 2010; Heslop et al., 2014; Jovane et al., 2012; Roberts et al., 2012). Magnetic measurements were made using a Lake Shore Cryotronics Inc. vibrating sample magnetometer at the Centro Oceanográfico de Registros Estratigráficos (CORE) Laboratory, Instituto Oceanográfico, Universidade de São Paulo, Brazil.

3.3. Pore Water Chemistry

Holes were drilled into core liners at 10-cm stratigraphic intervals, and pore waters were extracted using Rhizon polymer filters with 0.1-μm pore size (Seeberg-Elverfeldt et al., 2005) connected to a syringe (http://www.rhizosphere.com/rhizons). A maximum of 10 ml of water was extracted for most samples. Soon after collection, ~2 ml of pore water was placed in a transparent glove box with an inert atmosphere for measuring dissolved oxygen (DO) concentration, pH, and oxidation-reduction potential (ORP). DO was measured with a DO probe connected to a VWR sympHony bench-top meter, while pH, EC, and ORP were measured with a HACH SensION portable meter. Detection limits are 0.03 mg/L (0.3%) for DO, 0.01 for pH, and 0.1 mV for ORP. Reproducibility tests performed with this equipment reveal that absolute values are not particularly consistent; however, measurements were made the same day under the same conditions, so data trends can be considered significant. All samples were filtered and diluted to 10 ml, with HNO_3 5% solution in ultrapure water (Milli-Q) and were analyzed using inductively coupled plasma optical emission spectrometry (ICP-OES). All 36 samples from cores 4 and 9 were filtered and diluted to 10 ml, with HNO_3 5% solution in ultrapure water (Milli-Q) in duplicates and were analyzed with ICP-OES using CASS-4 as reference material. The limits of detection of the HACH SensION (intended as the lowest amount that could be reliably detected in the sample) are 0.01 for pH and 0.1 mV for ORP, with reproducibility less than 3% and signal-to-noise ratios of 3. The precision of the measurement (intended as measuring error) is ≤0.01 for pH and ≥1 mV for ORP. On the other hand, the precision of the measurement intended as reproducibility is ±0.01 for pH and ±1 mV for ORP. Pore water analyses on sediments from Site 9 were carried out on a different gravity core to that used for other analyses because vibrations associated with coring are likely to have disturbed the pore fluid distribution.

3.4. Mineralogy, Grain Size, and Petrophysical Properties

Powder X-ray diffraction (XRD) analysis was carried out on samples collected at 10-cm stratigraphic intervals from Core 9 (40 samples were analyzed). Samples were prepared by crushing and pulverizing ~0.2 g

of bulk sediment in a mortar. Samples were analyzed with an Olympus® Benchtop XRD/XRF (BTX) diffractometer using Co-K radiation, operated at 30 kV and 0.326 mA, over the 2θ range of 5°–60°, with a step size of 0.05° (results are a stack of 60 exposures to X-rays, each of 15-s duration). Mineral identification and analysis was carried out using the XPowder software (Version 2010.01.15 PRO), which uses the PDF-2 International Centre for Diffraction Data database. XRD identification criteria are based on Biscaye (1965), Moore and Reynolds (1989), and Hillier et al. (2003). Semiquantitative analyses were performed through the reference intensity ratio method, which is based on scaling all data to diffractions from standard reference materials, according to Chung (1974). About 5 g of sample from 10-cm stratigraphic intervals were used for grain size analyses. Samples were treated with 10% hydrogen peroxide to remove organic matter, and with 0.05 g of pyrophosphate added to each sample to avoid clay mineral flocculation. The measurements were performed with a Bluewave Microtrac system. Petrophysical properties of Core 9 were measured using a GEOTEK multisensor core logger, with piezo-electric ceramic transducer for *P* wave velocity measurements, a Bartington Instruments loop sensor for magnetic susceptibility measurements, and natural gamma-ray counters for natural gamma-ray spectroscopy, density, and porosity measurements.

3.5. Transmission Electron Microscope Imaging

For transmission electron microscope (TEM) imaging, magnetic nanocrystals from Core 4 (at 0- to 30-, 45- to 60-, and 75- to 90-cm depths) and Core 9M (at 0- to 15-, 15- to 30-, 45- to 60-, and 90- to 105-cm depths) were extracted following Strehlau et al. (2014). After concentrating nanocrystals with a magnet, the material was deposited over formvar-coated 300 mesh copper grids and air dried. Images were obtained with a Morgagni TEM (FEI, Hillsboro, OR, United States) at 80 kV.

3.6. Radiocarbon Dating

Six bivalve shell specimens were chosen from Core 9M at depths of 54, 162, 220, 314, 320, and 409 cm for ^{14}C dating. All bivalves were closed, articulated, and in life position, with no evidence of transport and sediment reworking. The shells were sent to two external laboratories (ICA, Inc. and the Physics Department, University of Arizona) for radiocarbon dating using accelerator mass spectrometry.

4. Results

4.1. Sedimentation Rate

Although it was not possible to calibrate the radiocarbon results due to uncertain marine reservoir corrections in this environment, the obtained ages can be used to estimate the mean sedimentation rate for Core 9M. Results, as shown in Figure S1 and Table S1 in the supporting information, are consistent, regardless of the laboratory in which they were analyzed. The sedimentation rate was stable throughout Core 9M with a mean value of 1.15 m/kyr.

4.2. Environmental Magnetism

Downcore environmental magnetic variations for Core 9M indicate higher NRM, ARM, and IRM values in the uppermost 35 cm of the core (Figures 2b–2d). Parameter values then drop abruptly and remain almost constantly low, decreasing by a factor of 10 to 100. The S ratio (Figure 2e) gives information about the relative concentration of high and low coercivity minerals. Its mean value for the uppermost 35 cm is 0.97, below which it drops to 0.4 at 40 cm, and then returns to values of ~0.8 throughout the rest of the core. S ratio values are consistent with the dominance of magnetite, except at 40 cm, which is consistent with a dominance of hematite (Bloemendal et al., 1992; Frank & Nowaczyk, 2008). HIRM (Figure 2f), which provides information about the absolute concentration of high coercivity minerals, has similar characteristics to NRM, susceptibility, ARM, and IRM. Consistently high values of NRM, ARM, and IRM indicate high magnetic mineral concentrations. ARM/IRM is sensitive to magnetic grain size and high values indicate a high fraction of SD relative to coarser particles (Evans & Heller, 2003). The magnetic property shift below 40 cm is consistent with rapidly decreasing magnetic mineral concentrations and increased magnetic particle sizes. S ratio and magnetic grain size variations suggest that the transition is marked by increased relative contributions of high coercivity minerals (e.g., hematite).

IRM acquisition curves for discrete samples have different behavior above and below depths of 30–40 cm (Figures 3 and S5 and Table S2). Above this depth, samples can be fitted with four components: one has

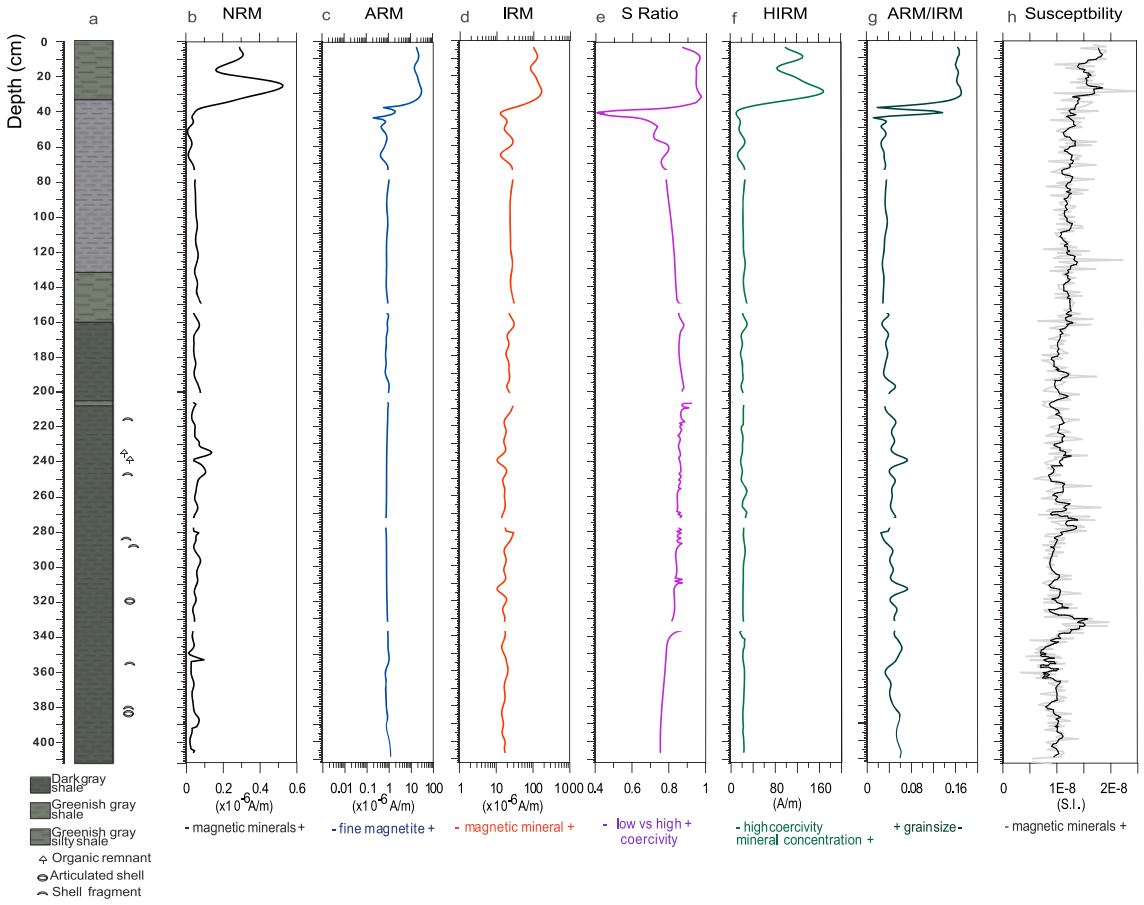

Figure 2. Downcore magnetic parameter variations for Core 9M. (a) Lithological log and (b–h) environmental magnetic parameters. Raw data for the low-field magnetic susceptibility curve (h) are shown in light gray, with a 3-point running average in black. Interpretations of parameter variations are indicated at the bottom of each panel. NRM = natural remanent magnetization; ARM = anhysteretic remanent magnetization; IRM = isothermal remanent magnetization.

low coercivity (average 8 mT) and high dispersion (0.31) that contributes 10% of the total signal and is interpreted to be detrital magnetite, or possibly the result of thermal activation of a superparamagnetic (SP) component within a broader SD distribution (Heslop et al., 2004). A component with high coercivity (242 mT) and dispersion of 0.25 is interpreted to be hematite, which contributes <4% of the magnetic signal. Two medium-coercivity components have values consistent with biogenic magnetite (mean coercivity of 32 mT and dispersion of 0.23, and mean coercivity of 61 mT and dispersion of 0.15), which together account for >84% of the magnetic signal of these samples. These components represent the BS and BH magnetite components, respectively, of Egli (2004b, 2004c). Below depths of 30–40 cm, samples are more variable in terms of magnetic component characteristics and number of components. The medium coercivity component has higher dispersion (>0.24), which indicates that the magnetite is either not biogenic or that the magnetite crystals have undergone some kind of alteration. Hematite contributions increase with depth to about 40 cm, and in some samples, a second high coercivity component appears, with a mean contribution of 8%. IRM acquisition curve decomposition for samples below 35 cm is nontrivial because of weak magnetizations and low signal-to-noise ratios due to low magnetic mineral concentrations.

IRM components in samples from Cores 1 and 4 are similar to those from Core 9M. Above the key transition depths (10 and 30 cm, respectively), samples are fitted with two components, one with low coercivity ($B_{1/2}$ of 14 mT) and one with medium coercivity ($B_{1/2}$ of 43 mT) and low dispersion parameter (DP) values, with the medium coercivity component contributing almost 80% of the IRM. Below these depths, samples are more variable, with a third high coercivity component ($B_{1/2}$ of 320 mT) that contributes >40% of the signal. The medium coercivity component has higher $B_{1/2}$ values in these samples, with a mean of 60 mT. The low

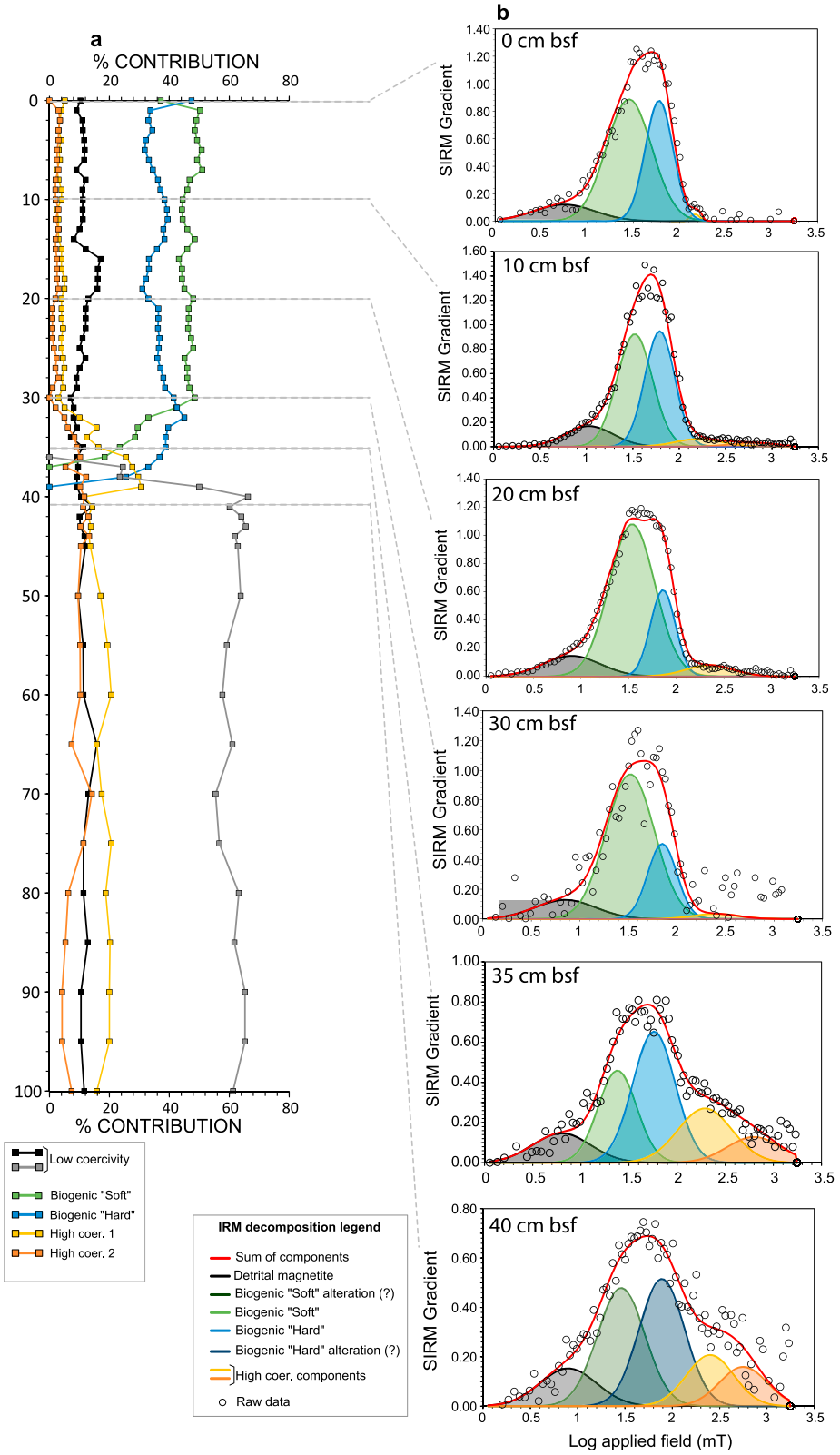

Figure 3. (a) Relative concentrations of magnetic minerals for the uppermost 100 cm of Core 9M from decomposition of isothermal remanent magnetization acquisition curves. (b) Gradient of isothermal remanent magnetization acquisition curves for representative samples at key depths; the raw data become increasingly noisy at lower depths due to low magnetic mineral concentrations.

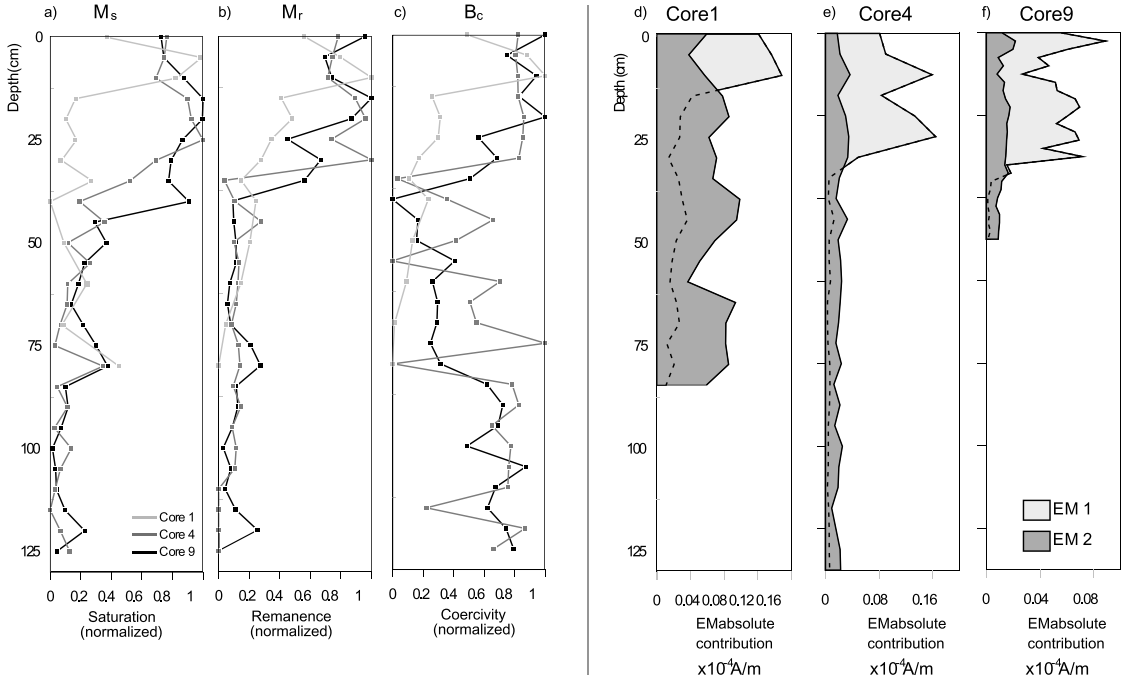

Figure 4. Magnetic hysteresis properties of Cores 1, 4, and 9M: (a) saturation magnetization (M_s), (b) saturation remanence (M_{rs}), and (c) coercivity (B_c). (d–f) Results of principal component analysis of low-resolution FORC diagrams for the three studied cores, expressed as the absolute contribution relative to the total magnetization: EM 1 is noninteracting SD magnetite, and EM 2 is SP/SD material. See text for discussion. Hysteresis parameters are normalized to indicate relative variations rather than absolute values. FORC EMs were defined using the FORCem algorithm of Lascu et al. (2015). FORC = first-order reversal curve; EM = end-member; SP = superparamagnetic.

coercivity component can be interpreted as coarse detrital magnetite (Egli, 2004a; Savian et al., 2014). Coercivity and DP values for the second component are consistent with the narrow grain size range of biogenic magnetite produced in situ by magnetotactic bacteria (Egli, 2004b, 2004c; Jovane et al., 2012; Kruiver & Passier, 2001; Roberts et al., 2012; Savian et al., 2014). The higher DP and coercivity distribution of this component below 30 and 40 cm may be due to alteration of biogenic magnetite. The high coercivity component values are consistent with the presence of hematite.

Hysteresis loops have low coercivities that are typical of magnetite (e.g., Dunlop & Özdemir, 1997). M_{rs} and M_s vary with similar trends as the magnetic concentration-dependent parameters in Figure 2, with high values above 35 cm and lower values below, while B_c decreases to a minimum at 40 cm and then increases downcore to reach similar values as in the upper part of the core at about 100 cm (Figures 4a–4c). Coercivity and magnetization parameters for Cores 1 and 4 have similar behavior and parameter values as Core 9M, with minimum values at depths of 10 and 30 cm, respectively. Coercivity increases again to reach similar values to those of surficial sediments below these depths (Figures 4a–4c).

Roberts, Tauxe, et al. (2018) presented extensive arguments for why the widely used Day diagram (Day et al., 1977) is ambiguous for domain state diagnosis. In doing so, they presented several examples where data trends in M_{rs}/M_s–B_{cr}/B_c space can provide valuable information about environmental processes even though regions of the Day diagram in which most data lie are not necessarily indicative of the domain state of constituent magnetic particles. Progressive downcore magnetite dissolution is one such example. Hysteresis parameters for samples from the uppermost 31 cm of Core 9M are clustered with M_{rs}/M_s values in the 0.23–0.37 range (Figure 5). From depths of 32 to 55 cm below sea floor (bsf), data are more dispersed, with a trend toward higher B_{cr}/B_c values and M_{rs}/M_s values of ~0.18. Below depths of 60 cm bsf, a looping trend is observed to higher M_{rs}/M_s values and slightly lower B_{cr}/B_c values that do not reach initial values for the uppermost part of the core. The anticlockwise loop of hysteresis ratios fits a model where reductive diagenesis leads to selective dissolution of the finest (biogenic) magnetic particles within an initial detrital + biogenic magnetic mineral assemblage, which results in a relatively coarser residual assemblage, while reaction of diagenetically released iron with sulfide in the sulfidic diagenetic zone produces authigenic

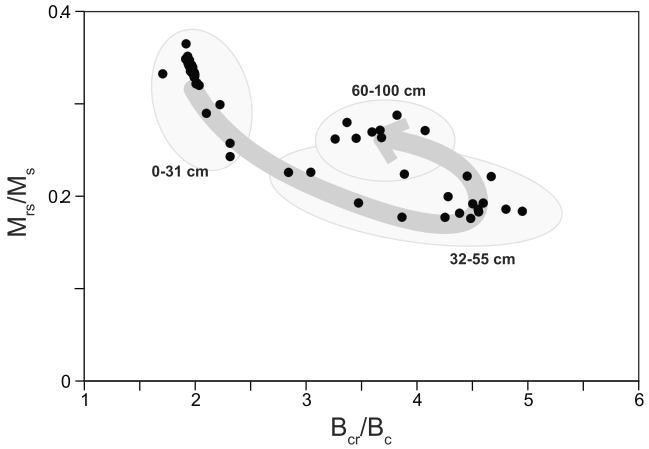

Figure 5. Plot of hysteresis parameters (M_{rs}/M_s versus B_{cr}/B_c; Day et al., 1977) to illustrate diagenetic trends for samples from the uppermost 100 cm of Core 9M. The gray arrow indicates a trend from higher B_{cr}/B_c values between 32 and 55 cm bsf, followed by a return to lower B_{cr}/B_c values and higher M_{rs}/M_s values below 60 cm bsf. See text for discussion and Rowan et al. (2009) for interpretation.

SP/SD greigite that causes the trend to loop back to higher M_{rs}/M_s values. This trend has been associated with progressive reductive diagenesis of shallow organic-rich sediments around the world (Roberts, 2015; Rowan et al., 2009), including the Oman, northern California, Oregon, and Argentine margins, Korea Strait, Ontong-Java Plateau, Niger Fan, and Japan Sea (Dillon & Bleil, 2006; Garming et al., 2005; Karlin, 1990; Liu et al., 2004; Rowan et al., 2009; Tarduno, 1994, 1995; Yamazaki et al., 2003). The magnetization of sediments in the sulfidic zone in which greigite is proposed to grow is weak (Roberts, Zhao, et al., 2018), so greigite has not always been detected in this zone. Its presence here is associated with the looping trend in M_{rs}/M_s–B_{cr}/B_c space rather than by direct identification.

High-resolution FORC diagrams for selected samples from Core 9M (Figure 6) have a distinct narrow horizontal central ridge that extends from near $B_c = 0$ to maximum values at ~30–40 mT, with negligible magnetostatic interactions (vertical axis). This ridge is prominent only in the uppermost 35 cm of the core. FORC diagrams for samples from Cores 1 and 4 contain a similar central ridge for samples from the uppermost parts of the cores, which disappear at depths of 10 and 30 cm, respectively (Figures S2–S4). Below this depth, only a SP component is visible (cf. Pike et al., 2001).

PCA analyses for the entire FORC data set are reported in Figure 4d for Core 1, Figure 4e for Core 4, and Figure 4f for Core 9M. The total low-resolution FORC signature can be divided into two end-members (EMs): one (EM 1) is consistent with noninteracting biogenic magnetite and a second (EM 2) represents SP material of possible detrital or diagenetic origin as discussed below. Downcore variations of the two EMs are consistent with the observation that key changes occur at depths of 10, 30, and 35 cm in Cores 1, 4, and 9M, respectively. Above these depths, the major constituent is biogenic magnetite, which makes up 80% of the magnetic signal. Below these depths, the biogenic magnetite signal disappears abruptly, and only a component close to the SP/SD threshold remains. Absolute values for each PCA EM and the total magnetization intensity indicate that while the biogenic component disappears with increasing depth, the SP/SD component is almost constant along the three cores. In addition, detrital magnetic mineral abundances are higher for Core 1 than for Cores 4 and 9M, which suggests that detrital input is higher in the outer part of Mamanguá Ría and that the waters of the internal part are relatively isolated from Ilha Grande Bay. Direct evidence of the presence of biogenic magnetite was obtained through TEM imaging of nanocrystals from magnetic mineral extracts (Figure 7).

4.3. Pore Water Chemistry

Pore water chemistry was analyzed on longer gravity cores from Site 4 (210 cm) and on a shorter core from Site 9 (170 cm) because vibracoring is likely to disturb the sedimentary pore water zonation. DO and ORP for the two cores (Figures 8a and 8b) have higher values in the uppermost 35 to 45 cm and lower values in the lower part of the cores. The downcore patterns are consistent at both sites. However, at Site 4 the values decrease more gradually to a minimum at 35 cm, while at Site 9 they drop sharply below 50 cm. Mean values for DO and ORP for Core 4 are 2.65 mg/L and −171 mV, respectively, for the uppermost 30 cm of the core, while from this depth to the bottom, mean values are 0.80 mg/L and −291 mV. Values for the uppermost 40 cm of Core 9 are 3.37 mg/L for DO and 146 mV for ORP, while from 40 cm to the bottom they are 0.72 mg/L and −272 mV, respectively. Dissolved pore water iron contents for Cores 4 and 9 are shown in Figure 8c. Values are fairly constant along the cores (with spikes in the upper part of Core 9, probably due to measurement errors associated with the small amounts of water extracted at these depths), with mean values of 4.6 μmol/L for Core 4 and 8.0 μmol/L for Core 9.

4.4. Mineralogy, Grain Size, and Petrophysical Properties

XRD patterns indicate the presence of four principal mineral phases: quartz, Na-feldspar, kaolinite, and illite (Figure 9b). The proportion of these phases does not vary significantly downcore, with mean concentrations

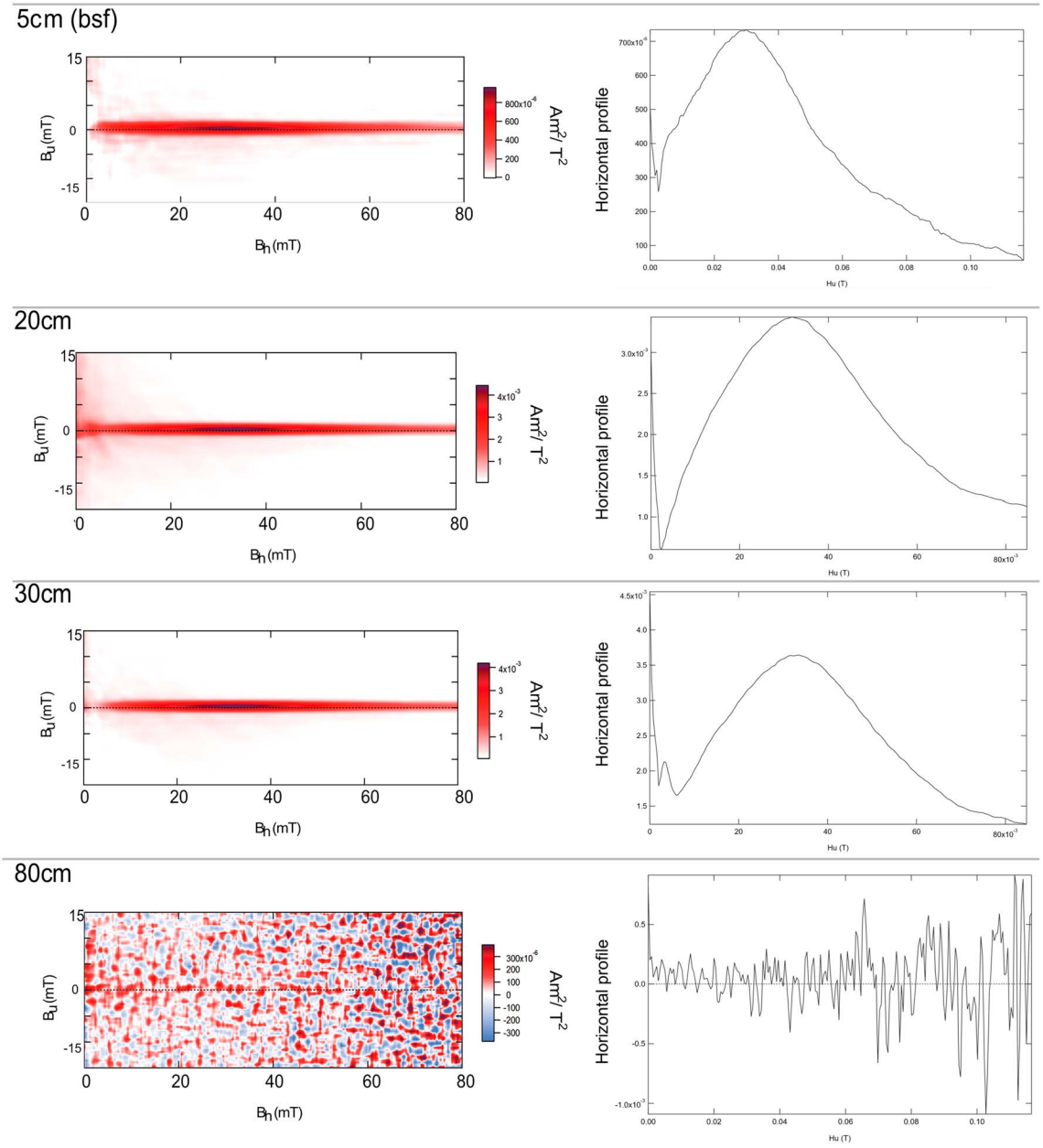

Figure 6. First-order reversal curve diagrams for four representative samples from Core 9M. Measurement parameters are as follows: $B_{c1} = 0$ mT and $B_{c2} = 110$ mT; $B_{u1} = -15$ mT and $B_{u2} = +15$ mT (297 curves) for a stack of five sets of measurements. The vertical profiles to the right are from along the $B_u = 0$ mT axis.

of 45%, 23%, 12%, and 20%, respectively. This constant mineralogical composition suggests that sediment provenance did not change throughout the studied time interval. Grain size analyses indicate that the sediment is composed predominantly of clay and silt, with a small sand fraction (Figure 6c). Downcore variations are minimal, with few intervals with slightly greater sand contents.

The mean *p* wave velocity is 1437 m/s for most of the core, although it is slightly lower in the upper 25 cm of sediment (Figure 9d) where sediment water contents are higher. Density follows the same pattern and increases from about 1.4 g/cm^3 to a steady value of 1.99 g/cm^3. Downcore volume normalized susceptibility values of the whole core are relatively stable at about 3.4 (microSI). Values decrease over ~20-cm intervals around core breaks due to measurement edge effects. Natural gamma rays have low counts per second (cps), with a mean value of 64.8 cps, and slightly higher counts (68) in the uppermost 5 cm of the core, and a maximum of 71 cps at 2.3 m bsf.

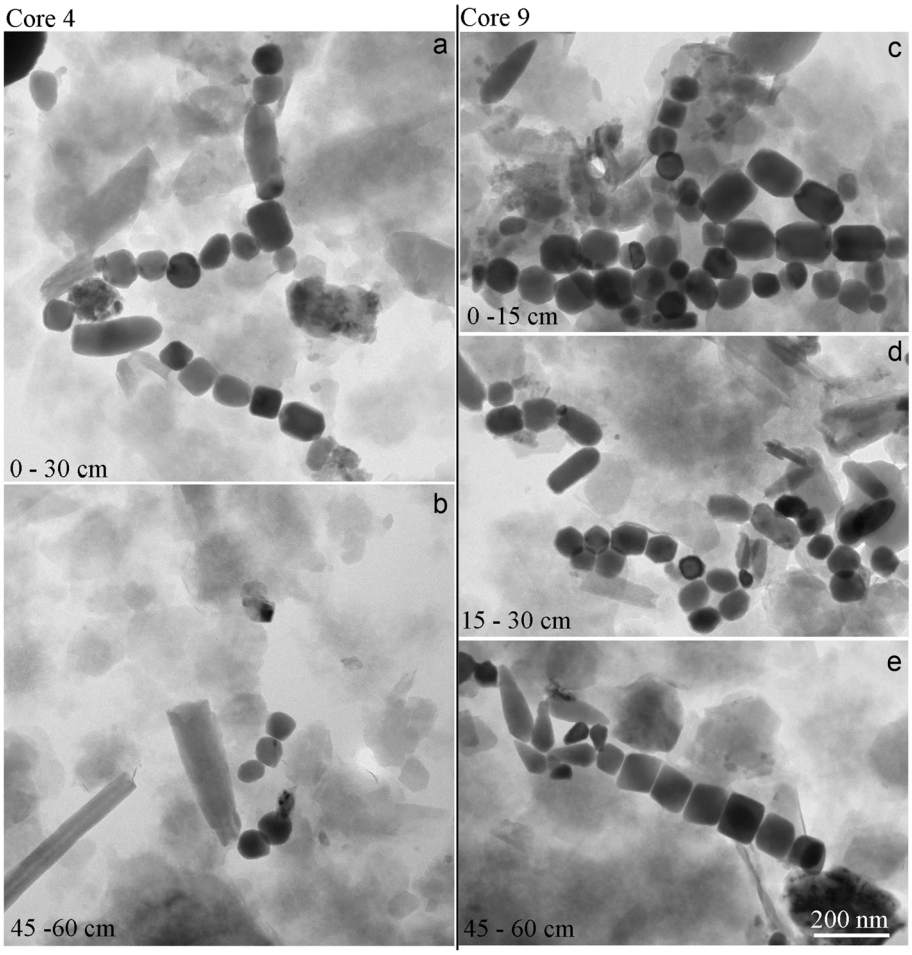

Figure 7. Transmission electron microscope images of nanocrystals extracted from sediments in Cores 4 and 9. The nanocrystals resemble magnetosomes based on their morphology and size. Nanocrystals with different shapes are observed at sediment depths of 0–30 cm in Core 4 and are not abundant in deeper layers from this core. Similar nanocrystals are observed at 0–60 cm in Core 9M, but not in deeper layers (90–105 cm). The scale bar in (e) is the same for all images.

5. Discussion

Environmental magnetic variations indicate that the uppermost 10–40 cm of sediment from Mamanguá Ría is rich in biogenic magnetite. This magnetite would have been produced in situ by MTB and is mixed with a small proportion of detrital magnetite and hematite sourced from weathering of local granites. Magnetite and hematite are also produced during pedogenesis, so that erosion and transportation of soil particles into the ría will contribute to sedimentary magnetism. High oxygen concentrations in the uppermost Mamanguá Ría sediment column cause oxidation of magnetite crystals, which is evident in synchrotron analyses that reveal progressive oxidation state changes of Fe (Rodelli et al., 2018). Magnetic analyses indicate little change from the magnetic signatures of pristine biogenic magnetite (Rodelli et al., 2018). This is mainly due to the fact that magnetosome crystals in living magnetotactic bacteria are encapsulated by a protein membrane (Bazylinski et al., 1993). Burial under oxidizing conditions will cause gradual oxidation of magnetite, but the magnetic properties and characteristic morphologies and sizes of magnetite magnetosomes remain detectable despite oxidation (e.g., Chang et al., 2013; Rodelli et al., 2018; Yamazaki & Shimono, 2013). In order to understand relationships between biogenic magnetite and the environments in which MTB lived, we assess variables that could have affected its formation and preservation. Lithological indicators (mineralogy, grain size, sediment density, and natural gamma ray analyses) and sedimentation rate are essentially constant along the studied cores, which means that variations in the concentration and characteristics of biogenic magnetite depend mostly on pore water chemistry. We assess these variables below.

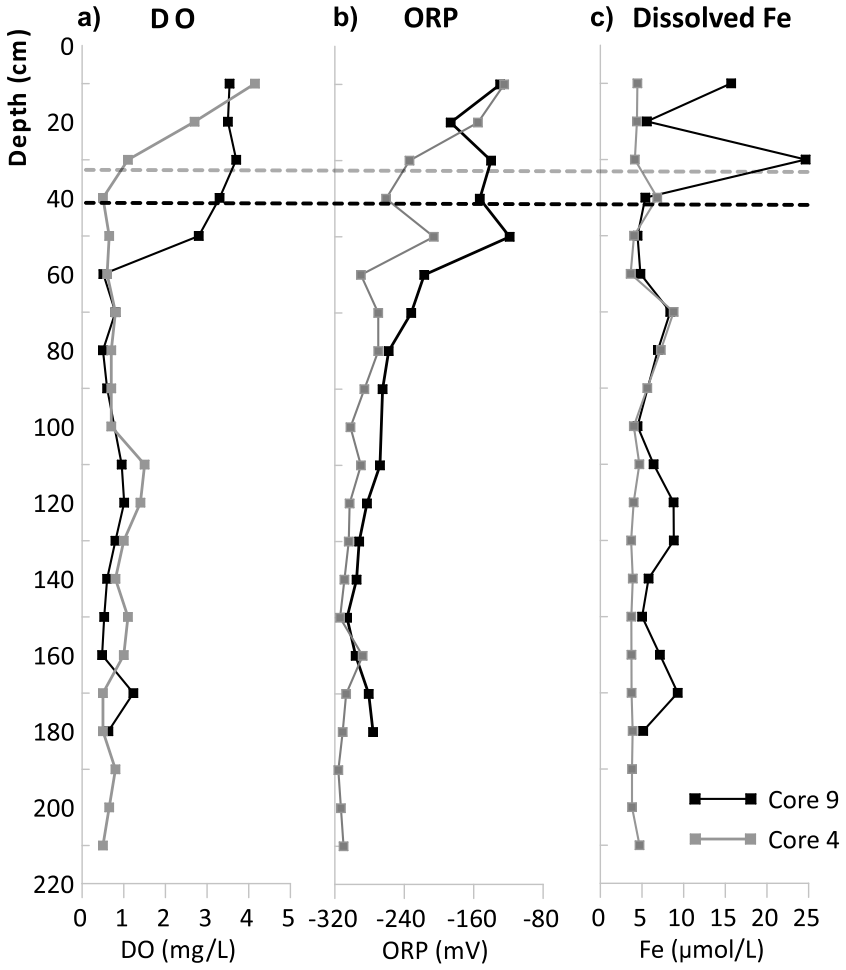

Figure 8. (a) Dissolved oxygen (DO), (b) oxidation-reduction potential (ORP), and (c) dissolved iron from pore waters extracted from Cores 4 and 9. The dark and light gray dashed lines indicate the inferred depths of the sulfate-methane transition in Cores 4 and 9, respectively. The limits of detection and quantification were 0.03 and 0.1 mmol/L, respectively, with reproducibility less than 3% and signal-to-noise ratios of 3.

5.1. MTB Response to Chemical Conditions

Dissolved oxygen and iron contents in the water column and pore waters are known limiting factors for magnetite biosynthesis (Liu et al., 2010; Mao et al., 2014), which also appear to be important for magnetite biomineralization in ancient MTB (Roberts et al., 2011). Sedimentation rate, detrital magnetic mineral abundance, mineralogy, sediment density, porosity, and grain size did not change significantly throughout deposition, so the external supply of key nutrients, such as Fe, is likely to have been relatively constant throughout the studied sediment. MTB thrive in environments with available dissolved Fe. The absence of biogenic magnetite at depths below 10, 30, and 35 cm in Cores 1, 4, 9, and 9M, respectively, is best explained by diagenetic reduction of oxygen within the sediment (Figure 5). Magnetite dissolution associated with Fe reduction should lead to increased dissolved Fe in pore waters, which is not observed in our data (apart from two Fe spikes in the upper part of Core 9, which are likely due to imprecise measurements). The lack of increased dissolved Fe with depth from the dissolution of biogenic magnetite is likely to be due to prompt Fe sequestration in insoluble pyrite in association with bacterial sulfate reduction within the sediment (Berner, 1984; Morse & Luther, 1999). The sulfide produced by these bacteria is a by-product of organic matter degradation (Berner, 1984; Charriau et al., 2011). However, we do not exclude the possibility that the lack of correlation between dissolved Fe and magnetosome dissolution could be related to (1) the fact that the amount of Fe sequestered by magnetosomes does not constitute a large fraction of the total Fe in

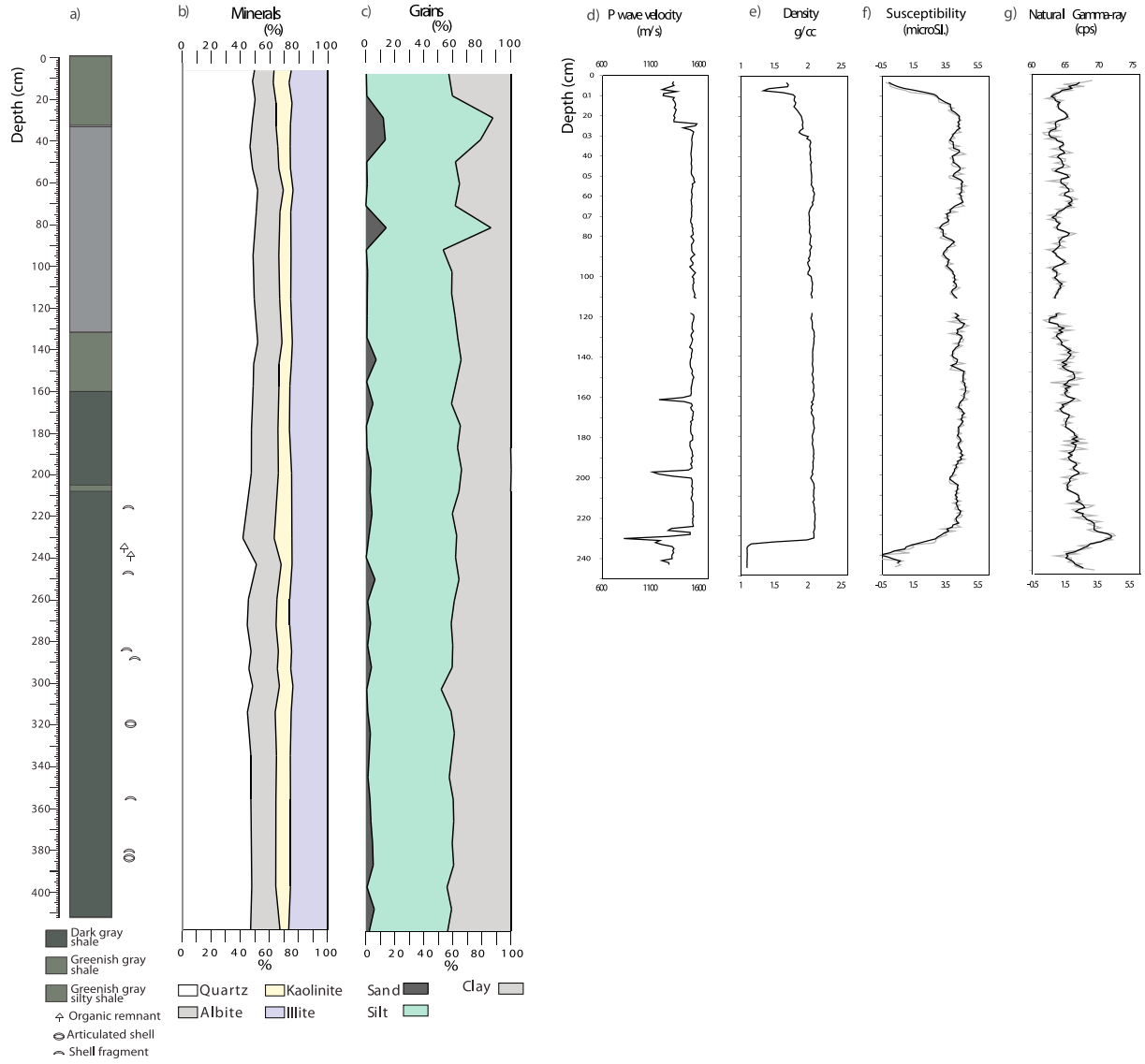

Figure 9. Bulk mineralogical and petrophysical property variations for two cores collected at Site 9. (a) Lithological log, (b) relative abundance of the four main mineral constituents (quartz, albite, kaolinite, and illite), (c) downcore grain size distribution variations expressed as a percentage of the total sediment of the core collected with a vibracorer (Core 9M), and (d–g) multisensor core logger downcore parameter variations for the core collected with a gravity corer (Core 9). Raw susceptibility and natural gamma ray data are shown in light gray, with a running 3-point average in black.

the system and (2) other processes that could result in iron take-up by products of extracellular dissimilatory iron-reducing or sulfate-reducing bacteria.

A stability diagram for Fe minerals as a function of pH and ORP (Pourbaix, 1974) is shown in Figure 10. Data for samples from the uppermost part of the cores fall within the stability area for Fe oxyhydroxides (e.g., goethite), which is indicative of oxic environments. Importantly, phospholipid membranes protect biogenic magnetite in living bacteria; therefore, MTB do not need to be in chemical equilibrium with their external environment. Data for sediments in Figure 10 lie on a trajectory with increasing depth that trends toward the stability area for Fe^{2+} in solution, which is indicative of progressive diagenetic reduction within the sediments. The oxygen gradient measured in the pore water profiles reflects organic matter decomposition, which consumes most of the oxygen within the uppermost tens of centimeters of sediment. This has a direct effect on biogenic magnetite preservation. A negative S ratio spike reflects a rapid relative increase in higher coercivity magnetic mineral contents (e.g., hematite), where the oxygen concentration decreases so rapidly

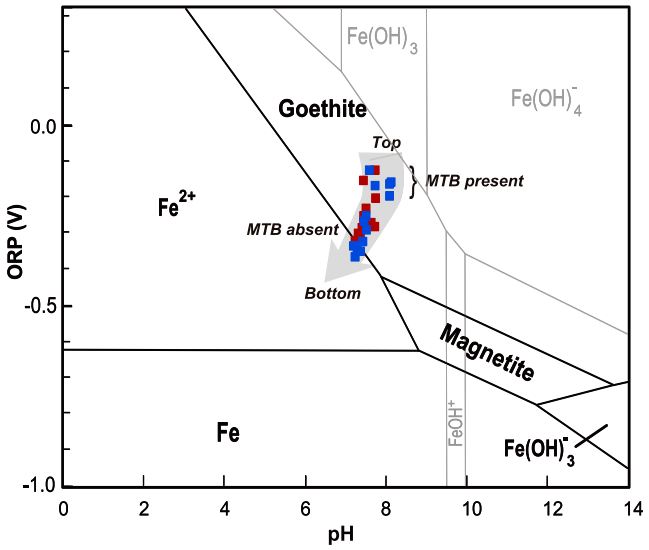

Figure 10. Diagram of pH versus oxidation-reduction potential for Fe in aqueous solution (Pourbaix, 1974) for Core 9 (blue squares) and Core 4 (red squares). The light gray arrow indicates the average trajectory, from core top to bottom, of pH versus ORP data.

that MTB cannot live and the interstitial sulfide content causes extensive biogenic magnetite dissolution. We consider this negative spike in the *S* ratio to represent the main sulfidic dissolution front that tends to occur just above the sulfate-methane transition (SMT; e.g., Riedinger et al., 2005). Hematite is slightly less reactive to sulfide than magnetite (Emiroglu et al., 2004; Garming et al., 2005; Kawamura et al., 2007; Liu et al., 2004; Poulton et al., 2004; Rey et al., 2005; Roberts, 2015; Robinson et al., 2000; Rowan et al., 2009; Yamazaki et al., 2003), so the observed local increase in hematite content is consistent with expectations of iron oxide reactivity to sulfide. Compared to deep-sea environments, it may seem unusual for molecular oxygen to still be present at this depth at which reductive organic matter respiration is occurring. Significant overlap in diagenetic zones is a feature of coastal environments (e.g., Canfield & Thamdrup, 2009), or it may be that the pore water profiles were disturbed by coring. Regardless, the progressive downcore ORP decrease is a clear indicator of progressive reduction and that the diagenetic loss of biogenic magnetite is due to progressive reductive dissolution.

5.2. Selective Magnetofossil Dissolution

Yamazaki and Kawahata (1998) demonstrated that magnetite magnetofossil morphology depends on organic carbon flux to the seafloor, with more elongated morphologies occurring in less oxic environments and vice versa. Egli (2004a, 2004b, 2004c) demonstrated that in lake sediments, BS and BH magnetite behave differently in environments with low oxygen concentrations (BH is more stable than BS). The difference between BS and BH lies in the shape of the crystals: the BS component is dominated by equant octahedra and the BH component is dominated by elongated parallelepipeds. More widespread evidence from marine sediments now links BS and BH magnetite to variable particle elongation with different MTB species thriving in different oxygen concentrations (e.g., Chang et al., 2013, 2018; Usui et al., 2017; Yamazaki, 2012; Yamazaki & Shimono, 2013).

Depth variations of BS and BH magnetite in sediments of Mamanguá Ría provide direct insights into the diagenetic fate of these magnetite types from a pore water based redox zonation in a modern depositional environment. The BS magnetite component is dominant down to 30 cm bsf and then diminishes rapidly before disappearing at 36 cm bsf. The concentration of BH magnetite, as expected, starts to increase at 29 cm bsf before reaching a maximum at 33 cm and then disappearing 3 cm deeper that the BS component at 39 cm bsf. New coercivity components appear in the IRM acquisition curves as soon as the BS and BH components disappear (Figure 3). These new components have almost the same mean coercivity values as the BS and BH components, but with larger dispersion. This behavior indicates that the sulfidic diagenetic front at which magnetite dissolution is occurring lies at 36–39 cm bsf, which is above the inferred position of the SMT at ~50–60 cm bsf. We cannot rule out the presence of MTB below the SMT based solely on magnetic properties because these measurements only reflect the presence of magnetic material, and MTB could pass undetected if internal metabolic processes consume most or all of the intracellular magnetite.

In addition to biogenic magnetite, the second magnetic mineral component identified from FORC-PCA is due to particles near the SP/SD threshold size (Figures 4d–4f). The SP particles in these sediments have two likely sources. First, SP maghemite and magnetite are common products of pedogenesis (e.g., Liu et al., 2007; Maher & Thompson, 1991; Verosub et al., 1993; Zhou et al., 1990), so that erosion and deposition of soil particles into the ría is an obvious source of SP particles. Second, reductive diagenesis produces authigenic SP particles (Tarduno, 1995) that are identified routinely in sulfidic diagenetic environments and are interpreted to be due to greigite (Rowan et al., 2009; Roberts, Zhao, et al., 2018). The possibility that the SP crystals might be of extracellular origin (e.g., Kato, 2016; Osorio et al., 2013) may be ruled out because no sign of extracellular magnetite is observed in TEM images. Both of the first two particle sources are likely to contribute to SP behavior in the studied cores. Soil particles are the most likely source of SP behavior in the oxic uppermost sediments, but their high surface area means that they will, like biogenic magnetite, dissolve readily under sulfidic conditions. Pedogenic SP particles are, therefore, highly unlikely to survive

below the sulfidic dissolution front. The presence of authigenic greigite in our samples below the sulfidic dissolution front is inferred from anticlockwise looping of hysteresis parameters in a plot of M_{rs}/M_s versus B_{cr}/B_c. SP greigite is likely produced below this depth; we interpret it to be responsible for the SP signal in the lower parts of the studied cores. It is curious that the SP signal is roughly constant above and below the sulfidic dissolution front in each core (Figures 4d–4f), but we consider the dual source of SP signals to be necessary given the contrasting stability of fine iron oxides and sulfides in oxic and sulfidic environments.

Process studies of modern diagenetic environments, such as the one presented here, are needed to understand mineral magnetic results in the context of changing pore water chemistry. Studies of the geological record typically lack such direct constraints and require the framework provided by modern process studies. Overall, our results provide valuable insights into the stability of biogenic magnetite under reducing conditions and are consistent with a well-known broader framework for mineral magnetic changes that occur in sediments during progressive diagenesis from oxic through to methanic conditions (e.g., Roberts, 2015). The relative stabilities of the frequently identified BS and BH components of Egli (2004a, 2004b, 2004c) have been discussed frequently in relation to varying diagenetic conditions (e.g., Chang et al., 2013, 2018; Egli, 2004a, 2004b, 2004c; Kodama et al., 2013; Usui et al., 2017; Yamazaki, 2012; Yamazaki & Shimono, 2013). However, inferences about the stability of these magnetite phases is based in all cases on diagenetic zonations based on magnetic properties with none of these studies including downcore pore water chemistry profiles. Our results provide an important direct constraint that validates such interpretations of magnetosome morphology and coercivity in terms of sediment oxygenation.

6. Conclusions

We demonstrate a correlation between environmental chemical conditions and magnetic minerals in surface sediments from Mamanguá Ría, Brazil. Sediment supply did not change significantly throughout the studied short sediment cores, so that sediment composition and relative nutrient abundances are likely to have been almost constant. Sedimentary oxygen content and redox potential, which were measured for pore waters from the studied sediments, therefore, provide the main factors that control the presence or absence of living magnetite-producing magnetotactic bacteria and magnetite magnetofossil preservation. Biogenic magnetite is present only where the redox potential and dissolved oxygen concentrations are high enough to allow magnetite-producing magnetotactic bacteria to live. The abrupt transition between relatively well-oxygenated and oxygen-depleted sediment is marked by the death of magnetite-producing magnetotactic bacteria and by rapid magnetosome dissolution. In the microaerobic surface environment, magnetotactic bacteria that produce both the biogenic soft and hard components of Egli (2004a, 2004b, 2004c) are present. With increasing depth over a narrow stratigraphic interval, the biogenic soft component is removed preferentially by reductive dissolution and only the hard component remains. This confirms that the biogenic hard component is more resistant to diagenetic dissolution than the biogenic soft component. At the sulfidic dissolution front, the remaining biogenic hard component dissolves and no biogenic magnetite is detected below this transition. At this transition, magnetite dissolution liberates dissolved Fe^{2+} that then becomes bioavailable for use by other chemosynthetic organisms or for reaction to form inorganic phases such as sedimentary greigite or pyrite. Overall, our results provide an important direct constraint that validates interpretations of magnetosome morphology and coercivity in terms of sediment oxygenation and redox potential.

Acknowledgments
D. R. and L. J. acknowledge funding from FAPESP grants 2012/212123 and 2011/22018-3, respectively. F. A. acknowledges funding from FAPERJ, CNPq, and CAPES. A. P. R. acknowledges funding from the Australian Research Council (grants DP140104544 and DP160100805). We are grateful for use of the following microscopy facilities: Unidade de Microscopia Multiusuário Souto-Padrón & Lins (UniMicro, IMPPG-UFRJ) and Centro Nacional de Biologia Estrutural e Bioimagem (CENABIO, UFRJ). We thank the Associate Editor and Liao Chang and Bruce Moskowitz for helpful review comments that improved the paper. Data presented in this study are listed in the supporting information.

References

Almeida, F. F. M. (1977). O cráton São Francisco (in Portuguese). *Revista Brasileira de Geociencias*, *7*, 349–379.

Bazylinski, D. A., & Frankel, R. B. (2004). Magnetosome formation in prokaryotes. *Nature Reviews Microbiology*, *2*(3), 217–230. https://doi.org/10.1038/nrmicro842

Bazylinski, D. A., Frankel, R. B., Heywood, B. R., Mann, S., King, J. W., Donaghay, P. L., & Hanson, A. K. (1995). Controlled biomineralization of magnetite (Fe_3O_4) and greigite (Fe_3S_4) in a magnetotactic bacterium. *Applied and Environmental Microbiology*, *61*(9), 3232–3239.

Bazylinski, D. A., Heywood, B. R., Mann, S., & Frankel, R. B. (1993). Fe_3O_4 and Fe_3S_4 in a bacterium. *Nature*, *366*(6452), 218. https://doi.org/10.1038/366218a0

Bazylinski, D. A., & Williams, T. J. (2006). Ecophysiology of magnetotactic bacteria. In *Magnetoreception and magnetosomes in bacteria* (pp. 37–75). Berlin, Heidelberg: Springer.

Benites, M., Pavani, D. A., de los Santos Maly, M., & Jovane, L. (2015). Shallow gas occurence in a Brazilian Ría (Saco do Mamangua, Rio de Janeiro), inferred from high resolution seismic data. *Continental Shelf Research*, *108*, 89–96. https://doi.org/10.1016/j.csr.2015.08.022

Bernardes, R. A. (1996). Estrutura e dinâmica da ictiofauna do Saco do Mamanguá (Paraty-RJ). Universidade de São Paulo (in Portuguese).
Berner, R. A. (1984). Sedimentary pyrite formation: An update. *Geochimica et Cosmochimica Acta*, *48*(4), 605–615. https://doi.org/10.1016/0016-7037(84)90089-9
Biscaye, P. E. (1965). Mineralogy and sedimentation of recent deep-sea clay in the Atlantic Ocean and adjacent seas and oceans. *Geological Society of America Bulletin*, *76*(7), 803–832. https://doi.org/10.1130/0016-7606(1965)76[803:MASORD]2.0.CO;2
Bloemendal, J., King, J. W., Hall, F. R., & Doh, S.-J. (1992). Rock magnetism of Late Neogene and Pleistocene deep-sea sediments: Relationship to sediment source, diagenetic processes, and sediment lithology. *Journal of Geophysical Research Atmospheres*, *97*(B4), 4361–4375. https://doi.org/10.1029/91JB03068
Canfield, D. E., & Thamdrup, B. (2009). Towards a consistent classification scheme for geochemical environments, or, why we wish the term 'suboxic' would go away. *Geobiology*, *7*(4), 385–392. https://doi.org/10.1111/j.1472-4669.2009.00214.x
Castaing, P., & Guilcher, A. (1995). Geomorphology and sedimentology of Rías. In G. M. E. Perillo (Ed.), *Geomorphology and sedimentology of estuaries* (pp. 69–111). Amsterdam: Elsevier. https://doi.org/10.1590/S0102-261x2004000100006
Chang, L., Harrison, R. J., Zeng, F., Berndt, T., Roberts, A. P., Heslop, D., & Zhao, X. (2018). Coupled microbial bloom and oxygenation decline recorded by magnetofossils during the Paleocene-Eocene Thermal Maximum. *Nature Communications*, *9*(1), 4007. https://doi.org/10.1038/s41467-18-06472-y
Chang, L., Winklhofer, M., Roberts, A. P., Heslop, D., Florindo, F., Dekkers, M. J., et al. (2013). Low-temperature magnetic properties of pelagic carbonates: Oxidation of biogenic magnetite and identification of magnetosome chains. *Journal of Geophysical Research: Solid Earth*, *118*, 6049–6065. https://doi.org/10.1002/2013JB010381
Charriau, A., Lesven, L., Gao, Y., Leermakers, M., Baeyens, W., Ouddane, B., & Billon, G. (2011). Trace metal behaviour in riverine sediments: Role of organic matter and sulfides. *Applied Geochemistry*, *26*(1), 80–90. https://doi.org/10.1016/j.apgeochem.2010.11.005
Chen, A. P., Berounsky, V. M., Chan, M. K., Blackford, M. G., Cady, C., Moskowitz, B. M., et al. (2014). Magnetic properties of uncultivated magnetotactic bacteria and their contribution to a stratified estuary iron cycle. *Nature Communications*, *5*(1), 4797. https://doi.org/10.1038/ncomms5797
Chung, F. H. (1974). Quantitative interpretation of X-ray diffraction patterns of mixtures. II. Adiabatic principle of X-ray diffraction analysis of mixtures. *Journal of Applied Crystallography*, *7*(6), 526–531. https://doi.org/10.1107/S0021889874010387
Day, R., Fuller, M., & Schmidt, V. A. (1977). Hysteresis properties of titanomagnetites: Grain-size and compositional dependence. *Physics of the Earth and Planetary Interiors*, *13*(4), 260–267. https://doi.org/10.1016/0031-9201(77)90108-X
Dillon, M., & Bleil, U. (2006). Rock magnetic signatures in diagenetically altered sediments from the Niger deep-sea fan. *Journal of Geophysical Research*, *111*, B03105. https://doi.org/10.1029/2004JB003540
Dunlop, D. J., & Özdemir, Ö. (1997). *Rock magnetism—Fundamentals and frontiers* (p. 573). New York: Cambridge University Press. https://doi.org/10.1017/CBO9780511612794
Egli, R. (2004a). Characterization of individual rock magnetic components by analysis of remanence curves. *Physics and Chemistry of the Earth*, *29*(13-14), 851–867. https://doi.org/10.1016/j.pce.2004.04.001
Egli, R. (2004b). Characterization of individual rock magnetic components by analysis of remanence curves: 2. Fundamental properties of coercivity distribution. *Physics and Chemistry of the Earth*, *29*(13–14), 851–867. https://doi.org/10.1016/j.pce.2004.04.001
Egli, R. (2004c). Characterization of individual rock magnetic components by analysis of remanence curves: 3. Bacterial magnetite and natural processes in lakes. *Physics and Chemistry of the Earth*, *29*(13-14), 869–884.https://doi.org/10.1016/j.pce.2004.03.010
Egli, R., Chen, A. P., Winklhofer, M., Kodama, K. P., & Horng, C. S. (2010). Detection of noninteracting single domain particles using first-order reversal curve diagrams. *Geochemistry, Geophysics, Geosystems*, *11*, Q01Z11. https://doi.org/10.1029/2009GC002916
Emiroglu, S., Rey, D., & Petersen, N. (2004). Magnetic properties of sediment in the Ria de Arousa (Spain): Dissolution of iron oxides and formation of iron sulphides. *Physics and Chemistry of the Earth*, *29*(13-14), 947–959. https://doi.org/10.1016/j.pce.2004.03.012
Evans, M. E., & Heller, F. (2003). *Environmental magnetism. Principles and applications of enviromagnetics* (Chap. 2, pp. 99). San Diego, CA: Academic Press.
Frank, U., & Nowaczyk, N. R. (2008). Mineral magnetic properties of artificial samples systematically mixed from haematite and magnetite. *Geophysical Journal International*, *175*(2), 449–461. https://doi.org/10.1111/j.1365-246X.2008.03821.x
Garming, J. F. L., Bleil, U., & Riedinger, N. (2005). Alteration of magnetic mineralogy at the sulfate–methane transition: Analysis of sediments from the Argentine continental slope. *Physics of the Earth and Planetary Interiors*, *151*(3-4), 290–308. https://doi.org/10.1016/j.pepi.2005.04.001
Harrison, R. J., & Feinberg, J. M. (2008). FORCinel: An improved algorithm for calculating first-order reversal curve distributions using locally weighted regression smoothing. *Geochemistry, Geophysics, Geosystems*, *9*, Q05016. https://doi.org/10.1029/2008GC001987
Heslop, D., McIntosh, G., & Dekkers, M. J. (2004). Using time- and temperature-dependent Preisach models to investigate the limitations of modelling isothermal remanent magnetization acquisition curves with cumulative log Gaussian functions. *Geophysical Journal International*, *157*, 55–63. https://doi.org/10.1111/j.1365-246X.2004.02155.x
Heslop, D., Roberts, A. P., & Chang, L. (2014). Recognition of biogenic magnetite components from first-order reversal curve signatures. *Geochemistry, Geophysics, Geosystems*, *15*, 2170–2179. https://doi.org/10.1002/2014GC005291
Hillier, S., Roe, M. J., Geelhoed, J. S., Fraser, A. R., Farmer, J. G., & Paterson, E. (2003). Role of quantitative mineralogical analysis in the investigation of sites contaminated by chromite ore processing residue. *Science of the Total Environment*, *308*(1–3), 195–210. https://doi.org/10.1016/S0048-9697(02)00680-0
Jovane, L., Florindo, F., Bazylinski, D. A., & Lins, U. (2012). Prismatic magnetite magnetosomes from cultivated *Magnetovibrio blakemorei* strain MV-1: A magnetic fingerprint in marine sediments? *Environmental Microbiology Reports*, *4*(6), 664–668. https://doi.org/10.1111/1758-2229.12000
Jovane, L., Herrero-Bervera, E., Hinnov, L. A., & Housen, B. A. (2013). *Magnetic methods and the timing of geological processes*, *Geological Society of London, Special Publications* (p. 373). London: The Geological Society of London.
Karlin, R. (1990). Magnetic mineral diagenesis in suboxic sediments at Bettis site W-N, NE Pacific Ocean. *Journal of Geophysical Research*, *95*(B4), 4421–4436. https://doi.org/10.1029/JB095iB04p04421
Kato, S. (2016). Microbial extracellular electron transfer and its relevance to iron corrosion. *Microbial Biotechnology*, *9*(2), 141–148. https://doi.org/10.1111/1751-7915.12340
Kawamura, N., Oda, H., Ikehara, K., Yamazaki, T., Shioi, K., Taga, S., et al. (2007). Diagenetic effect on magnetic properties of marine core sediments from the southern Okhotsk Sea. *Earth, Planets and Space*, *59*(2), 83–93. https://doi.org/10.1186/BF03352680
Kirschvink, J. L. (1980). The least-squares line and plane and the analysis of palaeomagnetic data. *Geophysical Journal of the Royal Astronomical Society*, *62*(3), 699–718. https://doi.org/10.1111/j.1365-246X.1980.tb02601.x

Kodama, K. P., Moeller, R. E., Bazylinski, D. A., Kopp, R. E., & Chen, A. P. (2013). The mineral magnetic record of magnetofossils in recent lake sediments of Lake Ely, PA. *Global and Planetary Change*, *110*, 350–363. https://doi.org/10.1016/j.gloplacha.2013.03.012

Kopp, R. E., & Kirschvink, J. L. (2008). The identification and biogeochemical interpretation of fossil magnetotactic bacteria. *Earth-Science Reviews*, *86*(1-4), 42–61. https://doi.org/10.1016/j.earscirev.2007.08.001

Kruiver, P. P., & Passier, H. F. (2001). Coercivity analysis of magnetic phases in sapropel S1 related to variations in redox conditions, including an investigation of the S ratio. *Geochemistry, Geophysics, Geosystems*, *2*(12). https://doi.org/10.1029/2001GC000181

Lascu, I., Harrison, R. J., Li, Y. T., Muraszko, J. R., Channell, J. E. T., Piotrowski, A. M., & Hodell, D. A. (2015). Magnetic unmixing of first-order reversal curve diagrams using principal component analysis. *Geochemistry, Geophysics, Geosystems*, *16*, 2900–2915. https://doi.org/10.1002/2015GC005909

Liu, J., Zhu, R. X., Roberts, A. P., Li, S. Q., & Chang, J. H. (2004). High-resolution analysis of early diagenetic effects on magnetic minerals in post-middle-Holocene continental shelf sediments from the Korea Strait. *Journal of Geophysical Research*, *109*, B03103. https://doi.org/10.1029/2003JB002813

Liu, Q. S., Deng, C. L., Torrent, J., & Zhu, R. X. (2007). Review of recent developments in mineral magnetism of the Chinese loess. *Quaternary Science Reviews*, *26*(3-4), 368–385. https://doi.org/10.1016/j.quascirev.2006.08.004

Liu, Q. S., Roberts, A. P., Larrasoaña, J. C., Banerjee, S. K., Guyodo, Y., Tauxe, L., & Oldfield, F. (2012). Environmental magnetism: Principles and applications. *Reviews of Geophysics*, *50*, RG4002. https://doi.org/10.1029/2012RG000393

Liu, Y., Li, G. R., Guo, F. F., Li, Y., & Li, L. J. (2010). Large-scale production of magnetosomes by chemostat culture of *Magnetospirillum gryphiswaldense* at high cell density. *Microbial Cell Factories*, *9*(1), 99. https://doi.org/10.1186/1475-2859-9-99

Maher, B. A., & Thompson, R. (1991). Mineral magnetic record of the Chinese loess and paleosols. *Geology*, *19*(1), 3–6. https://doi.org/10.1130/0091-7613(1991)019<0003:MMROTC>2.3.CO;2

Mann, S., Frankel, R. B., & Blakemore, R. P. (1984). Structure, morphology and crystal growth of bacterial magnetite. *Nature*, *310*(5976), 405–407. https://doi.org/10.1038/310405a0

Mao, X., Egli, R., Petersen, N., Hanzlik, M., & Zhao, X. (2014). Magnetotaxis and acquisition of detrital remanent magnetization by magnetotactic bacteria in natural sediment: First experimental results and theory. *Geochemistry, Geophysics, Geosystems*, *15*, 255–283. https://doi.org/10.1002/2013GC005034

Mohamed, K. J., Rey, D., Rubio, B., Dekkers, M. J., Roberts, A. P., & Vilas, F. (2011). Onshore-offshore gradient in reductive early diagenesis in coastal marine sediments of the Ria de Vigo, Northwest Iberian Peninsula. *Continental Shelf Research*, *31*(5), 433–447. https://doi.org/10.1016/j.csr.2010.06.006

Moore, D. M., & Reynolds, R. C. (1989). *X-ray diffraction and the identification and analysis of clay minerals* (Vol. 332). New York: Oxford University Press.

Morse, J. W., & Luther, G. (1999). Chemical influences on trace metal-sulfide interactions in anoxic sediments. *Geochimica et Cosmochimica Acta*, *63*(19-20), 3373–3378. https://doi.org/10.1016/S0016-7037(99)00258-6

Moskowitz, B. M., Frankel, R. B., & Bazylinski, D. A. (1993). Rock magnetic criteria for the detection of biogenic magnetite. *Earth and Planetary Science Letters*, *120*(3-4), 283–300. https://doi.org/10.1016/0012-821X(93)90245-5

Osorio, H., Mangold, S., Denis, Y., Ñancucheo, I., Esparza, M., Johnson, D. B., et al. (2013). Anaerobic sulfur metabolism coupled to dissimilatory iron reduction in the extremophile *Acidithiobacillus ferrooxidans*. *Applied and Environmental Microbiology*, *79*(7), 2172, AEM-03057–2181. https://doi.org/10.1128/AEM.03057-12

Pan, Y., Petersen, N., Davila, A. F., Zhang, L., Winklhofer, M., Liu, Q., et al. (2005). The detection of bacterial magnetite in recent sediments of Lake Chiemsee (southern Germany). *Earth and Planetary Science Letters*, *232*(1-2), 109–123. https://doi.org/10.1016/j.epsl.2005.01.006

Pan, Y., Petersen, N., Winklhofer, M., Davila, A. F., Liu, Q., Frederichs, T., et al. (2005). Rock magnetic properties of uncultured magnetotactic bacteria. *Earth and Planetary Science Letters*, *237*(3-4), 311–325. https://doi.org/10.1016/j.epsl.2005.06.029

Pedrosa-Soares, A. C., Noce, C. M., de Alkmin, F. F., da Silva, L. C., Bambinski, M., Cordani, U., & Castañeda, C. (2007). Orógeno Araçuaí: Síntese do conhecimento 30 anos após Almeida 1977. *Geonomos*, *15*(1), 1–16.

Pike, C. R., Roberts, A. P., & Verosub, K. L. (1999). Characterizing interactions in fine magnetic particle systems using first order reversal curves. *Journal of Applied Physics*, *85*(9), 6660–6667. https://doi.org/10.1063/1.370176

Pike, C. R., Roberts, A. P., & Verosub, K. L. (2001). First-order reversal curve diagrams and thermal relaxation effects in magnetic particles. *Geophysical Journal International*, *145*(3), 721–730. https://doi.org/10.1046/j.0956-540x.2001.01419.x

Poulton, S. W., Krom, M. D., & Raiswell, R. (2004). A revised scheme for the reactivity of iron (oxyhydr)oxide minerals towards dissolved sulfide. *Geochimica et Cosmochimica Acta*, *68*(18), 3703–3715. https://doi.org/10.1016/j.gca.2004.03.012

Pourbaix, M. (1974). *Atlas of electrochemical equilibria in aqueous solutions* (2nd English ed.). Houston, TX: National Association of Corrosion Engineers.

Rey, D., Mohamed, K. J., Bernabeu, A., Rubio, B., & Vilas, F. (2005). Early diagenesis of magnetic minerals in marine transitional environments: Geochemical signatures of hydrodynamic forcing. *Marine Geology*, *215*(3-4), 215–236. https://doi.org/10.1016/j.margeo.2004.12.001

Riedinger, N., Pfeifer, K., Kasten, S., Garming, L. F. L., Vogt, C., & Hensen, C. (2005). Diagenetic alteration of magnetic signals by anaerobic oxidation of methane related to a change in sedimentation rate. *Geochimica et Cosmochimica Acta*, *69*(16), 4117–4126. https://doi.org/10.1016/j.gca.2005.02.004

Roberts, A. P. (2015). Magnetic mineral diagenesis. *Earth-Science Reviews*, *151*, 1–47. https://doi.org/10.1016/j.earscirev.2015.09.010

Roberts, A. P., Almeida, T. P., Church, N. S., Harrison, R. J., Heslop, D., Li, Y. L., et al. (2017). Resolving the origin of pseudo-single domain magnetic behavior. *Journal of Geophysical Research: Solid Earth*, *122*, 9534–9558. https://doi.org/10.1002/2017JB014860

Roberts, A. P., Chang, L., Heslop, D., Florindo, F., & Larrasoaña, J. C. (2012). Searching for single domain magnetite in the "pseudosingle domain" sedimentary haystack: Implications of biogenic magnetite preservation for sediment magnetism and relative paleointensity determinations. *Journal of Geophysical Research*, *117*, B08104. https://doi.org/10.1029/2012JB009412

Roberts, A. P., Florindo, F., Villa, G., Chang, L., Jovane, L., Bohaty, S. M., et al. (2011). Magnetotactic bacterial abundance in pelagic marine environments is limited by organic carbon flux and availability of dissolved iron. *Earth and Planetary Science Letters*, *310*(3-4), 441–452. https://doi.org/10.1016/j.epsl.2011.08.011

Roberts, A. P., Pike, C. R., & Verosub, K. L. (2000). First-order reversal curve diagrams: A new tool for characterizing the magnetic properties of natural samples. *Journal of Geophysical Research*, *105*(B12), 28,461–28,475. https://doi.org/10.1029/2000JB900326

Roberts, A. P., Tauxe, L., Heslop, D., Zhao, X., & Jiang, Z. X. (2018). A critical appraisal of the "Day" diagram. *Journal of Geophysical Research: Solid Earth*, *123*(4), 2618–2644. https://doi.org/10.1002/2017JB015247

Roberts, A. P., Zhao, X., Harrison, R. J., Heslop, D., Muxworthy, A. R., Rowan, C. J., et al. (2018). Signatures of reductive magnetic mineral diagenesis from unmixing of first-order reversal curves. *Journal of Geophysical Research: Solid Earth*, *123*(6), 4500–4522. https://doi.org/10.1029/2018JB015706

Robertson, D. J., & France, D. E. (1994). Discrimination of remanence-carrying minerals in mixtures, using isothermal remanent magnetisation acquisition curves. *Physics of the Earth and Planetary Interiors*, *82*(3–4), 223–234.

Robinson, S. G., Sahota, J. T. S., & Oldfield, F. (2000). Early diagenesis in North Atlantic abyssal plain sediments characterized by rock-magnetic and geochemical indices. *Marine Geology*, *163*(1-4), 77–107. https://doi.org/10.1016/S0025-3227(99)00108-5

Rodelli, D., Jovane, L., Roberts, A. P., Cypriano, J., Abreu, F., & Lins, U. (2018). Fingerprints of partial oxidation of biogenic magnetite from cultivated and natural marine magnetotactic bacteria using synchrotron radiation. *Environmental Microbiology Reports*, *10*(3), 337–343. https://doi.org/10.1111/1758-2229.12644

Rowan, C. J., Roberts, A. P., & Broadbent, T. (2009). Reductive diagenesis, magnetite dissolution, greigite growth and paleomagnetic smoothing in marine sediments: A new view. *Earth and Planetary Science Letters*, *277*(1-2), 223–235. https://doi.org/10.1016/j.epsl.2008.10.016

Savian, J. F., Jovane, L., Frontalini, F., Trindade, R. I. F., Coccioni, R., Bohaty, S. M., et al. (2014). Enhanced primary productivity and magnetotactic bacterial production in response to middle Eocene warming in the Neo-Tethys Ocean. *Palaeogeography Palaeoclimatology Palaeoecology*, *414*, 32–45. https://doi.org/10.1016/j.palaeo.2014.08.009

Savian, J. F., Jovane, L., Giorgioni, M., Iacoviello, F., Rodelli, D., Roberts, A. P., et al. (2016). Environmental magnetic implications of magnetofossil occurrence during the Middle Eocene Climatic Optimum (MECO) in pelagic sediments from the equatorial Indian Ocean. *Palaeogeography Palaeoclimatology Palaeoecology*, *441*, 212–222. https://doi.org/10.1016/j.palaeo.2015.06.029

Seeberg-Elverfeldt, J., Schlüter, M., Feseker, T., & Kölling, M. (2005). Rhizon sampling of porewaters near the sediment-water interface of aquatic systems. *Limnology and Oceanography: Methods*, *3*, 361–371.

Spera, A. (2012). Registro de variações ambientais dos últimos 3000 anos da Região da Ria do Mamanguá, Rio de Janeiro, utilizando marcadores orgânicos moleculares. Universidade de São Paulo.

Strehlau, J. H., Hegner, L. A., Strauss, B. E., Feinberg, J. M., & Penn, R. L. (2014). Simple and efficient separation of magnetic minerals from speleothems and other carbonates. *Journal of Sedimentary Research*, *84*(11), 1096–1106. https://doi.org/10.2110/jsr.2014.89

Tarduno, J. A. (1994). Temporal trends of magnetic dissolution in the pelagic realm: Gauging paleoproductivity? *Earth and Planetary Science Letters*, *123*(1–3), 39–48. https://doi.org/10.1016/0012-821X(94)90255-0

Tarduno, J. A. (1995). Superparamagnetism and reduction diagenesis in pelagic sediments—Enhancement or depletion? *Geophysical Research Letters*, *22*(11), 1337–1340. https://doi.org/10.1029/95GL00888

Teixeira, C. L. (2009). Caracterização do sedimento superficial de enseadas da Baía da Ilha Grande-RJ, com ênfase na distribuição espacial de metais (in Portuguese). Universidade Federal Fluminense.

Usui, Y., Yamazaki, T., & Saitoh, M. (2017). Changing abundance of magnetofossil morphologies in pelagic red clay around Minamitorishima, Western North Pacific. *Geochemistry, Geophysics, Geosystems*, *18*, 4558–4572. https://doi.org/10.1002/2017GC007127

Verosub, K. L., Fine, P., Singer, M. J., & TenPas, J. (1993). Pedogenesis and paleoclimate: Interpretation of the magnetic susceptibility record of Chinese loess-paleosol sequences. *Geology*, *21*(11), 1011–1014. https://doi.org/10.1130/0091-7613(1993)021<1011:PAPIOT>2.3.CO;2

Verosub, K. L., & Roberts, A. P. (1995). Environmental magnetism: Past, present, and future. *Journal of Geophysical Research*, *100*(B2), 2175–2192. https://doi.org/10.1029/94JB02713

Weeks, R., Laj, C., Endignoux, L., Fuller, M., Roberts, A., Manganne, R., et al. (1993). Improvements in long-core measurement techniques: Applications in palaeomagnetism and palaeoceanography. *Geophysical Journal International*, *114*(3), 651–662. https://doi.org/10.1111/j.1365-246X.1993.tb06994.x

Xuan, C., & Channell, J. E. T. (2009). UPmag: MATLAB software for viewing and processing u channel or other pass-through paleomagnetic data. *Geochemistry, Geophysics, Geosystems*, *10*, Q10Y07. https://doi.org/10.1029/2009GC002584

Yamazaki, T. (2012). Paleoposition of intertropical convergence zone in the eastern Pacific inferred from glacial-interglacial changes in terrigenous and biogenic magnetic mineral fractions. *Geology*, *40*(2), 151–154. https://doi.org/10.1130/G32646.1

Yamazaki, T., Abdeldayem, A. L., & Ikehara, K. (2003). Rock-magnetic changes with reduction diagenesis in Japan Sea sediments and preservation of geomagnetic secular variation in inclination during the last 30,000 years. *Earth, Planets and Space*, *55*(6), 327–340. https://doi.org/10.1186/BF03351766

Yamazaki, T., & Kawahata, H. (1998). Organic carbon flux controls the morphology of magnetofossils in marine sediments. *Geology*, *26*(12), 1064–1066. https://doi.org/10.1130/0091-7613(1998)026<1064:OCFCTM>2.3.CO;2

Yamazaki, T., & Shimono, T. (2013). Abundant bacterial magnetite occurrence in oxic red clay. *Geology*, *41*(11), 1191–1194. https://doi.org/10.1130/G34782.1

Yan, L., Zhang, S., Chen, P., Liu, H., Yin, H., & Li, H. (2012). Magnetotactic bacteria, magnetosomes and their application. *Microbiological Research*, *167*(9), 507–519. https://doi.org/10.1016/j.micres.2012.04.002

Zhou, L. P., Oldfield, F., Wintle, A. G., Robinson, S. G., & Wang, J. T. (1990). Partly pedogenic origin of magnetic variations in Chinese loess. *Nature*, *346*(6286), 737–739. https://doi.org/10.1038/346737a0

References From the Supporting Information

Marz, C., Meinhardt, K., Schnetger, B., & Brumsack, H. J. (2015). Silica diagenesis and benthic fluxes in the Arctic Ocean. *Marine Chemistry*, *171*, 1–9. https://doi.org/10.1016/j.marchem.2015.02.003